

Research Article

Multiscale Time Series Decomposition for Structural Dynamic Properties: Long-Term Trend and Ambient Interference

Xiaolei Chu ,^{1,2} Wei Cui ,^{1,3} Shengyi Xu,¹ Lin Zhao,^{1,3} Hua Guan,⁴ and Yaojun Ge^{1,3}

¹State Key Lab of Disaster Reduction in Civil Engineering, Tongji University, Shanghai 200092, China

²Department of Civil and Environmental Engineering, University of California, Berkeley, CA 94720, USA

³Key Laboratory of Transport Industry of Bridge Wind Resistance Technologies, Tongji University, Shanghai 200092, China

⁴Zhejiang Zhoushan Sea Crossing Bridge Co. Ltd, Zhoushan, Zhejiang 316031, China

Correspondence should be addressed to Wei Cui; cuiwei@tongji.edu.cn

Received 1 November 2022; Revised 9 January 2023; Accepted 16 January 2023; Published 9 February 2023

Academic Editor: Sara Casciati

Copyright © 2023 Xiaolei Chu et al. This is an open access article distributed under the Creative Commons Attribution License, which permits unrestricted use, distribution, and reproduction in any medium, provided the original work is properly cited.

In structural health monitoring (SHM), variations of structural dynamic properties are paramount to indicate the health status of structures. Structural dynamic properties are time variant due to various long-term effects (e.g., structural deterioration) and periodic effects (e.g., periodic variations of temperature, humidity, and traffic). Sometimes periodic effects will interfere with the quantification of long-term effects. Though important, there are still limited research studies aiming to distinguish these two effects. Given the amount of SHM data, it is possible to solve the issue from a data-driven perspective. This article proposes a time series decomposition methodology to divide the time series of structural dynamic properties into long-term parts, multiscale periodic parts, holiday parts, and error parts. We extract the 10-year dynamic properties of a long-span bridge using the fast Bayesian FFT identification algorithm and choose two dynamic modes of that bridge as examples to explain how our proposed methodology works. We use the long-term parts to extract the rules of structural deterioration. The multiscale periodic parts are utilized to find the relationships with the periodically varying ambient conditions (i.e., temperature and humidity) in different time scales (i.e., yearly, weekly, and daily). Then, the long-term and periodic effects can be distinguished. For the long-term effects, the modal frequencies tend to decrease but the damping ratios seem to increase. For the periodic effects, we find that the increment of temperature will lead to the decrease of both modal frequencies and damping ratios. The variations of modal frequencies induced by deterioration and temperature are of the same amplitudes. The variations of both modal frequencies and damping ratios are not significantly related with humidity. This article could provide references for damage detection and safety assessment for similar bridges.

1. Introduction

The structural health monitoring (SHM) system of critical infrastructures is very important, which makes it possible for researchers to identify and analyze the structural dynamic properties continuously. Operational modal analysis is prevailing these years because it can analyze SHM data without disturbing the normal service of structures. There are multiple operational modal identification technologies that have been investigated for output-only systems, such as frequency-domain decomposition (FDD) [1], wavelet [2, 3], and stochastic subspace identification (SSI) [4]. Recently, Bayesian system identification [5] has made significant

development, which viewed the modal identification as inference with plausible system models. For parameters that need to be inferred, Bayesian system identification can give both the most probable values (MPVs) and corresponding posterior uncertainty. Katafygiotis and Yuen [6] proposed a Bayesian spectral density approach for modal updating, where the power spectral density (PSD) of measured signals was used. Yuen and Katafygiotis [7] and Au [8, 9] developed the Bayesian FFT approach for modal updating, which directly utilized the statistical characteristics of the Fourier transform of measured signals. Both Bayesian spectral density approach and FFT approach have been successfully applied on issues of system identification [10–12]. In this

article, we will use the Bayesian FFT approach to extract 10-year dynamic properties of the Xihoumen Bridge in China.

Modal frequencies and damping ratios are important for structural integrity and safety. For example, the abnormal reduction of modal frequency is often regarded as an indicator of the loss of structural integrity, and Salawu [13] concluded that 5% reduction of modal frequency was a reliable sign for structural damage. As for damping ratio, it is the key parameter of long-span bridge's wind-resistant capacity, especially for the performance of vortex-induced vibration [14–16]. The reduction of damping ratio may lead to large-amplitude vortex-induced vibration [14]. In addition, in current engineering practices, the designed service life for critical infrastructures (e.g., long-span bridges) is over hundred years. Considering all reasons listed above, it is paramount for researchers to investigate how dynamic properties will change with time. Nevertheless, recent studies revealed that the fluctuating environmental conditions could also induce the significant changes of dynamic properties, which are not caused by structural damage. For example, Yuen and Kuok [17] monitored a 22-story reinforced concrete building for one year and found that with the increase of ambient temperature, the modal frequency of buildings would increase. For long-span bridges, however, Li et al. [18], Mao et al. [3], Anastasopoulos et al. [19], and Hwang et al. [20] found that the increase of ambient temperature would decrease the modal frequency, which was opposite to the varying rule of buildings. In conclusion, both long-term deterioration (due to structural damage) and varying ambient conditions can influence the modal frequencies and damping ratios. It is important to distinguish the effects of structural deterioration from ambient interference, but few research studies were found since the complicated inherent mechanisms. Thanks to the accumulation of SHM data, however, it is possible to distinguish them from a data-driven perspective. It should be stressed that damping ratio is fairly complicated and related with many factors (not just varying ambient temperature and humidity). For example, damping ratio can also be influenced by aerodynamic effects [18, 21], soil-structure interaction [22], and man-made changes (e.g., maintenance of expansion joints and tuned mass damper [23]). Due to the limitation of the length, this study only focuses on the relationship between structural dynamic properties (modal frequencies and damping ratios) and ambient interference (temperature and humidity).

There have been multiple applications of time series methods on the monitoring of civil infrastructures, mainly focusing on the detection of structural damage. For example, Omennetzer and Brownjohn [24] formulated a vector seasonal autoregressive integrated moving average (ARIMA) model to obtain information from the recorded strain signals and found that the changes in the ARIMA coefficients meant potential structural change and damage. Many research studies using the statistical characteristics of SHM data to classify and locate the damage are also investigated [25–28]. Explainable component analysis (i.e., long-term deterioration, seasonal fluctuation, and effects of special events) remains to be a formidable task either for researchers

or bridge maintainers. With the proliferation of SHM data, however, it is possible to quantify different components. The Prophet model developed by Facebook [29] is a good tool with interpretable parameters that can be intuitively adjusted by analysts with domain knowledge. The Prophet model used a decomposable time series model [30] with three main components: trend (i.e., structural deterioration in SHM), seasonality (which can be used for the analysis of ambient interference), and holidays (which can be used for explaining the anomaly in special events). In this paper, we used the Prophet model to distinguish and quantify the structural deterioration and ambient interference (temperature and relative humidity [31]) of Xihoumen Bridge, where the recorded acceleration data from 2012 ~ 2021 were employed.

The contents of this paper are organized as follows: In section 2, we briefly introduce the theoretical background of the fast Bayesian FFT identification algorithm and the layout of Xihoumen Bridge including the SHM systems; then, 10-year identified structural dynamic properties (modal frequencies and damping ratios) are presented. In section 3, we propose a multiscale time series decomposition methodology to distinguish the long-term part and periodic part of structural dynamic properties. In section 4 and section 5, we decompose the time series so that the effects of structural deterioration and ambient interference (relationships with temperature and relative humidity) are investigated. The amplitudes of the variations caused by structural deterioration and ambient interference are also investigated. In conclusion (section 7), this article employs a data-driven methodology to distinguish the effects of structural deterioration (i.e., structural damage) from ambient interference, which gives insights for future engineering practices.

2. Fast Bayesian FFT Identification Algorithm

2.1. Theoretical Background. If the acceleration time history measured at n DOFs of a structure is noted as $\{\hat{x}_j \in R^n: j = 1, \dots, N\}$ and abbreviated as $\{\hat{x}_j\}$, where N is the number of samples per channel, the FFT of $\{\hat{x}_j\}$ is defined as

$$\begin{aligned} \mathcal{F}_k &= \mathbf{F}_k + i\mathbf{G}_k \\ &= \sqrt{\frac{(2\Delta t)}{N}} \sum_{j=1}^N \hat{x}_j \exp \left\{ -2\pi i \left[\frac{(k-1)(j-1)}{N} \right] \right\}, \quad (k = 1, \dots, N), \end{aligned} \quad (1)$$

where $i^2 = -1$, Δt is the sampling interval, and $\mathbf{F}_k = \text{Re}\mathcal{F}_k$ and $\mathbf{G}_k = \text{Im}\mathcal{F}_k$ denote the real and imaginary part of the FFT, respectively. For $k = 2, 3, \dots, N_q$, the FFT corresponds to frequency $f_k = (k-1)/N\Delta t$. Here, $N_q = \text{int}[N/2] + 1$ ($\text{int}[\cdot]$ denotes the integer part) corresponds to the FFT ordinate at the Nyquist frequency. For modal identification, only these $(N_q - 1)$ FFT values are utilized.

In the context of Bayesian inference, the measured acceleration is modeled as $\hat{x}_j = \ddot{x}_j(\theta) + \epsilon_j$, where $\ddot{x}_j(\theta)$ is the acceleration response of the structural model defined by the

set of model parameters θ , the subject to be identified, and ϵ_j is the prediction error that accounts for the deviation between the model response and measured data, possibly owing to measurement noise and modeling error. Yuen and Katafygiotis [7] derived the joint PDF for the augmented FFT vectors $\{\mathbf{Z}_k = [\mathbf{F}_k^T, \mathbf{G}_k^T]^T \in R^{2n}: k = 2, \dots, N_q\}$ and applied it to Bayesian modal identification. For a high sampling rate and long duration of data, \mathbf{Z}_k is a zero-mean Gaussian vector with covariance matrix given by

$$\mathbf{C}_k = \frac{1}{2} \begin{bmatrix} \Phi(\text{Re}\mathbf{H}_k)\Phi^T & -\Phi(\text{Im}\mathbf{H}_k)\Phi^T \\ \Phi(\text{Im}\mathbf{H}_k)\Phi^T & \Phi(\text{Re}\mathbf{H}_k)\Phi^T \end{bmatrix} + \left(\frac{\sigma^2}{2}\right) \mathbf{I}_{2n}, \quad (2)$$

where $\Phi \in R^{n \times m}$ is the mode shape matrix confined to the measured DOFs (the i th column gives the i th mode shape), σ^2 is the (constant) spectral density level of the prediction error, \mathbf{I}_{2n} denotes the $2n \times 2n$ identity matrix, and \mathbf{H}_k is the

spectral density matrix of the model response and its (i, j) entry is given by

$$\mathbf{H}_k(i, j) = S_{ij} \left[(\beta_{ik}^2 - 1) + i(2\zeta_i \beta_{ik}) \right]^{-1} \left[(\beta_{jk}^2 - 1) - i(2\zeta_j \beta_{jk}) \right]^{-1}, \quad (3)$$

where $\beta_{ik} = f^{(i)}/f_k$ = frequency ratio, $f^{(i)}$ and ζ_i = natural frequency and damping ratio of the i th mode, respectively, and S_{ij} = cross-spectral density between the i th and j th modal excitation.

The set of modal parameters θ consists of modal frequencies, damping ratios, mode shapes, entries $\{S_{ij}\}$ of the spectral density matrix of modal excitations, and spectral density σ^2 of the prediction error. Assuming a non-informative prior distribution, the posterior PDF of θ has given that FFT data are proportional to the likelihood function $p(\{\mathbf{Z}_k\}|\theta)$

$$p(\theta|\{\mathbf{Z}_k\}) \propto p(\{\mathbf{Z}_k\}|\theta) = (2\pi)^{-(N_q-1)/2} \left[\prod_k \det \mathbf{C}_k(\theta) \right]^{-(1/2)} \times \exp \left[-\left(\frac{1}{2}\right) \sum_k \mathbf{Z}_k^T \mathbf{C}_k(\theta)^{-1} \mathbf{Z}_k \right], \quad (4)$$

where the dependence of \mathbf{C}_k on θ has been emphasized [32]. It is convenient to write with the negative log-likelihood function $L(\theta)$ form

$$p(\theta|\{\mathbf{Z}_k\}) \propto \exp[-L(\theta)], \quad (5)$$

where

$$L(\theta) = \frac{1}{2} \sum_k \left[\ln \det \mathbf{C}_k(\theta) + \mathbf{Z}_k^T \mathbf{C}_k(\theta)^{-1} \mathbf{Z}_k \right]. \quad (6)$$

Then, the most probable value (MPV) $\hat{\theta}$ is

$$\begin{aligned} \hat{\theta} &= \arg \max_{\theta} [p(\theta|\{\mathbf{Z}_k\})] \\ &= \arg \min_{\theta} [L(\theta)]. \end{aligned} \quad (7)$$

People can use simulated annealing [33], MCMC [34], or some other minimum-value searching methods to obtain $\hat{\theta}$. Simulated annealing is employed in this paper. The posterior covariance of $\hat{\theta}$ can also be quantified by Hessian matrix [32, 35], which is not the main focus of this paper and is not discussed here. Different from the traditional frequency-domain identification methods, the significant digits of the identified parameters here have no concern with the sampling duration. For example, the resolution of frequency in FFT analysis will be higher when the sampling duration is longer. In the Bayesian method, however, all parameters are obtained by optimization, where the probability serves as the metrics but not the sampling duration. So, the significant digits of dynamic properties in this paper can be more than the traditional methods'.

2.2. Bridge and Its Layout of SHM Systems. As shown in Figure 1, Xihoumen Bridge is a long-span suspension bridge with a 1650-meter central main span located at Zhoushan City, linking Jintang Island and Cezi Island.

In Xihoumen Bridge's SHM system shown in Figure 2, AC10 ~ AC18 are the servo accelerometers (ACs). The sampling rate of ACs is 50 Hz. ACs can record accelerations of vertical and lateral directions of the bridge's cross section. AC12, AC15, and AC18 are for lateral accelerations. The other ACs are for vertical accelerations. Vertical and torsional modes are of primary interests here. As a result, we only utilize the vertical acceleration data but abandon the lateral ones. In this study, we use 6 synchronously measured acceleration data in vertical directions (i.e., AC10, AC11, AC13, AC14, AC16, and AC17) to infer structural dynamic properties. Due to the huge amount of data, we divide the time history of acceleration hour by hour and then modal frequencies and damping ratios are identified hour by hour.

2.3. Details of Identification Processing. In this article, the long-term and continuous structural dynamic properties are identified from 2012 to 2021 by hour. Due to the limit of the article length, we only display the results of two dynamic modes to explain the methodology in this study: first, first-order symmetric torsional mode; second, fourth-order symmetric torsional mode [36]. Similar conclusions can also be found in other dynamic modes. Comparing the results of modal frequencies and damping ratios (as shown in section 3.5), we can notice that the damping ratios are much more discrete than modal frequencies. It is also found that the damping ratios from approximately September 2019 to May 2020 are anomalously higher than the others. The anomaly might be caused by some man-made actions (e.g., maintenance of expansion joints). The reason is out of the scope of this study and will not be discussed. For the analysis in section 3, the time series in the anomalous part are not utilized.

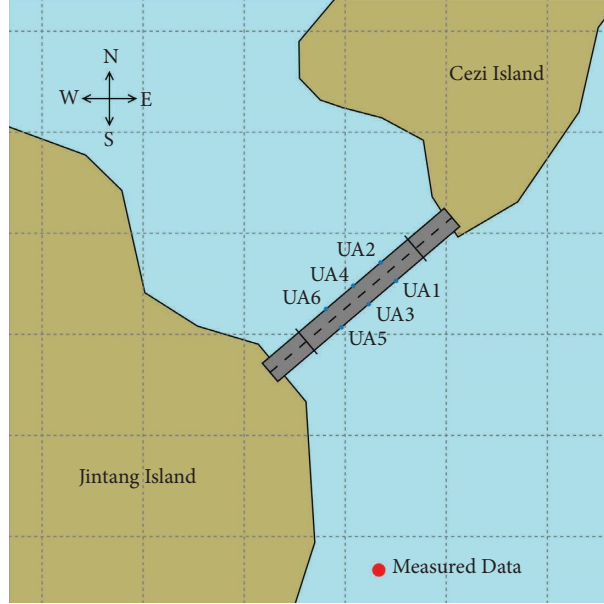


FIGURE 1: Location of Xihoumen Bridge.

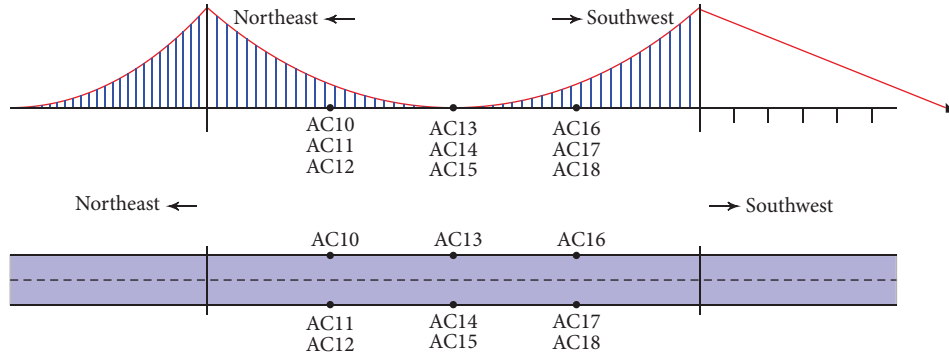


FIGURE 2: Layout of the SHM system of Xihoumen Bridge.

3. Multiscale Time Series Decomposition for Structural Dynamic Properties

The Prophet model was developed by Facebook team [29], which was an easily interpretable tool for time series analysis. For the real-world application, it is believed that the time series are periodically fluctuating due to the periodic ambient interference [30]. The Prophet model utilizes a decomposable and interpretable time series model with three main model components: trend, seasonality, and holidays. These three components are combined as follows:

$$y(t) = g(t) + s(t) + h(t) + \epsilon_t, \quad (8)$$

where $g(t)$ is the trend term which describes nonperiodic changes, $s(t)$ models periodic changes (e.g., daily, weekly, and yearly seasonality), $h(t)$ represents the effects of holidays that occur on specific days, and the error term ϵ_t means any idiosyncratic changes which are not properly accommodated by the model.

3.1. The Trend Model. Usually, there are two kinds of trend models that cover many real-world applications [29]: the saturating growth model and the piecewise linear model. For the application of a saturating growth model on SHM, it requires the domain knowledge for the rules of deterioration, which is usually case-specific and not general. As a result, a piecewise linear model is utilized in this study for convenience.

Because the growth rate of the trend model is not constant, there should be changepoints to incorporate a varying rate while fitting the historical data. Given S changepoints at times s_j , $j = 1, \dots, S$, a vector of rate adjustments $\delta \in \mathbb{R}^S$ is defined, where δ_j is the change in rate that occurs at time s_j . The rate at time t is the base rate k plus all of the adjustments up to that point: $k + \sum_{j: t > s_j} \delta_j$. Alternatively, we can define a vector $a(t) \in \{0, 1\}^S$ for the sake of concision:

$$a_j(t) = \begin{cases} 1, & \text{if } t \geq s_j, \\ 0, & \text{otherwise.} \end{cases} \quad (9)$$

Then, the rate at time t is $k + \mathbf{a}(t)^T \boldsymbol{\delta}$. The offset parameter m will be adjusted accordingly with varying k in order to connect the endpoints of the segments. The correct adjustment at changepoint j can be given as follows:

$$\gamma_j = \left(s_j - m - \sum_{l < j} \gamma_l \right) \left(1 - \frac{k + \sum_{l \leq j} \delta_l}{k + \sum_{l \leq j} \delta_l} \right). \quad (10)$$

Lastly, the trend model with linear trend is obtained as follows:

$$g(t) = (k + \mathbf{a}(t)^T \boldsymbol{\delta})t + (m + \mathbf{a}(t)^T \boldsymbol{\gamma}), \quad (11)$$

where k is the growth rate, $\boldsymbol{\delta}$ has the rate adjustments, m is the offset parameter, and γ_j is set to $-s_j \delta_j$ to make the function continuous.

With sufficient domain knowledge, the changepoints s_j can be specified by experts. Again, due to the limitation of domain knowledge, automatic selection of changepoints s_j is more practical, which is accomplished by putting a sparse prior on $\boldsymbol{\delta}$.

3.2. Seasonality. Time series that occur in the real-world often have multiscale seasonality as a result of periodically fluctuating ambient interference and the human behaviors. For example, a 24-hour duration can be a period because of the natural daily variation; one-year duration can also be a period since the condition of natural environment (e.g., temperature and humidity) varies by year. Another example of the human behaviors is that a 7-day work week can make effects on the time series that repeat each week since people's periodic work often counts week by week. To fit and forecast these effects, we usually specify seasonality models that are periodic functions of t .

Fourier series are employed here to provide a flexible model of periodic effects [37], which have both computational efficiency and interpretability. Assume P is the regular period we expect the time series to have (e.g., if the timescale is defined by day, $P = 365.25$ for yearly data and $P = 7$ for weekly data). For an arbitrary period P , its seasonal effects are obtained by the following equation:

$$s(t) = \sum_{n=1}^N \left(a_n \cos\left(\frac{2\pi n t}{P}\right) + b_n \sin\left(\frac{2\pi n t}{P}\right) \right). \quad (12)$$

Fitting seasonality requires estimating the $2N$ parameters $\beta = [a_1, b_1, \dots, a_N, b_N]^T$. This is done by constructing a matrix of seasonality vectors for each value of t in our historical and future data, for example, with weekly seasonality and $N = 3$:

$$X(t) = \left[\cos\left(\frac{2\pi(1)t}{7}\right), \dots, \sin\left(\frac{2\pi(3)t}{7}\right) \right]. \quad (13)$$

The seasonal component is then obtained as follows:

$$s(t) = X(t)\beta, \quad (14)$$

where β can be obtained by putting a sparse prior.

3.3. Holidays and Events. Holidays and events may make impacts on time series to some extent. For example, the structural dynamic properties may vary on holidays due to the heavier traffic condition [38]. In this study, we assume the effects of holidays and events are observed each year on New Year's Day, Chinese New Year, Tomb-Sweeping Day, Labor Day, Dragon Boat Festival, Mid-Autumn Festival, and National Day, as shown in Table 1.

For each holiday i , let D_i be the set of past and future dates for that holiday. We add an indicator function representing whether time t is during holiday i , and assign each holiday a parameter κ_i which is the corresponding change in the forecast. This is done in a similar way as seasonality by generating a matrix of regressors

$$Z(t) = [\mathbf{1}(t \in D_1), \dots, \mathbf{1}(t \in D_L)], \quad (15)$$

and taking

$$h(t) = Z(t)\kappa, \quad (16)$$

where κ can be obtained by putting a sparse prior.

3.4. Performance Metrics. We can evaluate the performance of our model by comparing the similarity of the estimated data with the historical data. In this study, we use the correlation coefficient as the metric

$$M = \sqrt{\frac{[n \sum_{i=1}^n y_i \hat{y}_i - (\sum_{i=1}^n y_i) \cdot (\sum_{i=1}^n \hat{y}_i)]^2}{[n \sum_{i=1}^n \hat{y}_i^2 - (\sum_{i=1}^n \hat{y}_i)^2] [n \sum_{i=1}^n y_i^2 - (\sum_{i=1}^n y_i)^2]}}, \quad (17)$$

where n is the number of time series, y_i is the real value (i.e., historical value), \hat{y}_i is the estimated value, and M is the performance metric. The closer M is to 1, the better the performance of the model is.

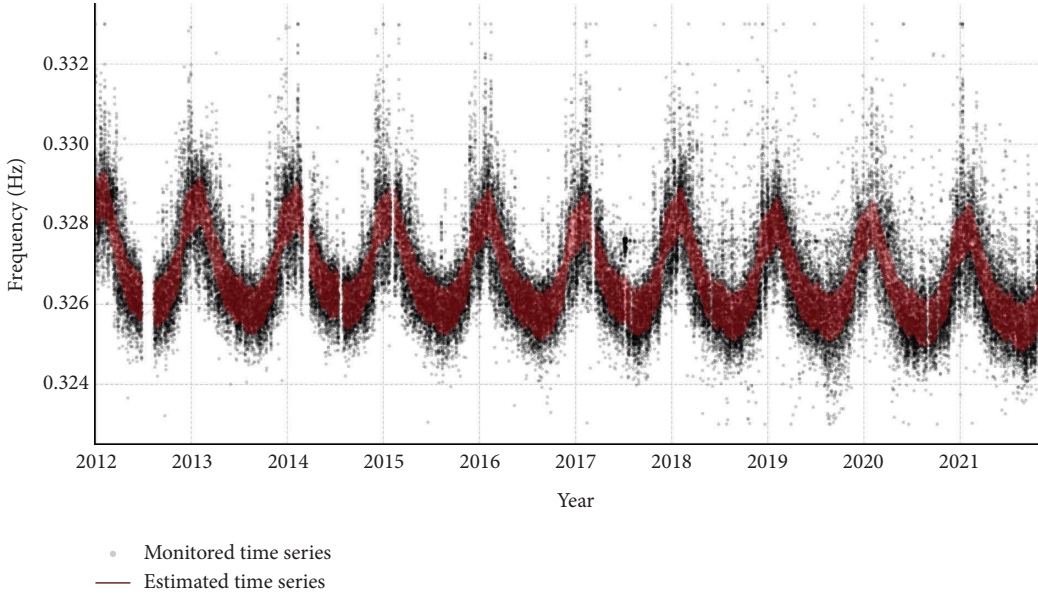
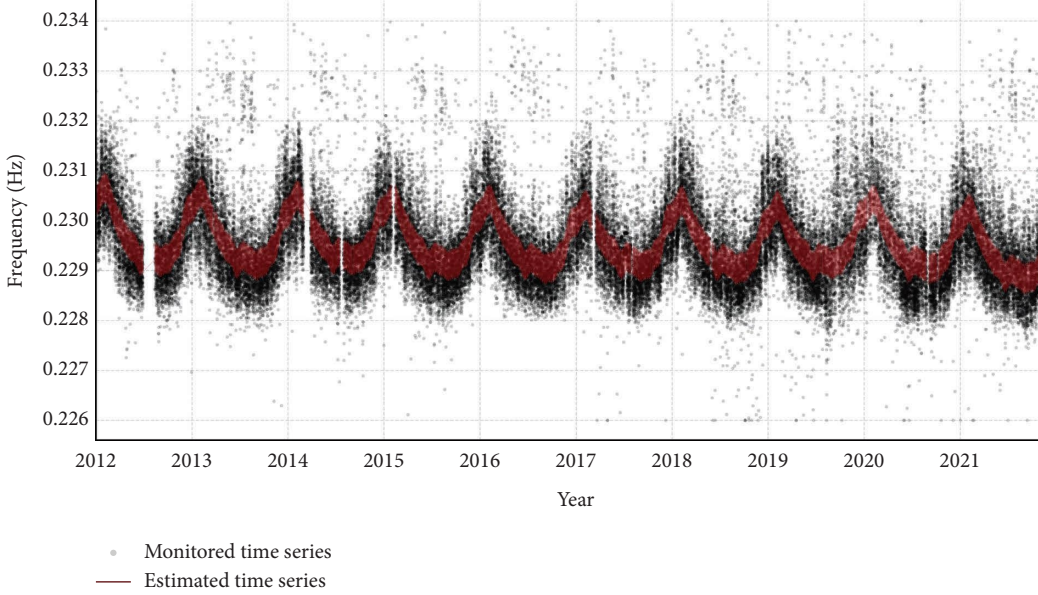
3.5. Identified Results. In this subsection, we choose the fourth-order symmetric torsional mode and the first-order torsional mode as examples to explain how the Prophet model works and to present the results of different timescale components. Modal frequency, damping ratio, and mode shapes are identified hour by hour. However, we do not find any obvious varying patterns for mode shapes. We only discuss modal frequencies and damping ratios here.

3.5.1. Decomposition for Modal Frequency. As shown in Figure 3, the black points are the identified time series of the modal frequency from the SHM system. The red points are the estimated time series, which are reconstructed by the Prophet model. The modal frequency exhibits an obvious yearly fluctuating phenomenon. Meanwhile, a general decreasing trend is also found.

As shown in Figure 4, the yearly fluctuation and general decreasing trend are also found in the first-order symmetric torsional mode.

TABLE 1: Examples of holidays in China.

Holiday	Country	Year	Date
New Year's Day	The whole world	2015	01.01–01.03
Chinese New Year	China	2015	02.19–02.24
Tomb-Sweeping Day	China	2015	04.04–04.06
Labor Day	China	2015	05.01–05.03
Dragon Boat Festival	China	2015	05.20–05.22
Mid-Autumn Festival	China	2015	09.26–09.27
National Day	China	2015	10.01–10.07
New Year's Day	The whole world	2016	01.01–01.03
...

FIGURE 3: Fourth-order symmetric torsional frequency: monitored time series and estimated time series ($M = 0.7999$).FIGURE 4: First-order symmetric torsional frequency: monitored time series and estimated time series ($M = 0.5997$).

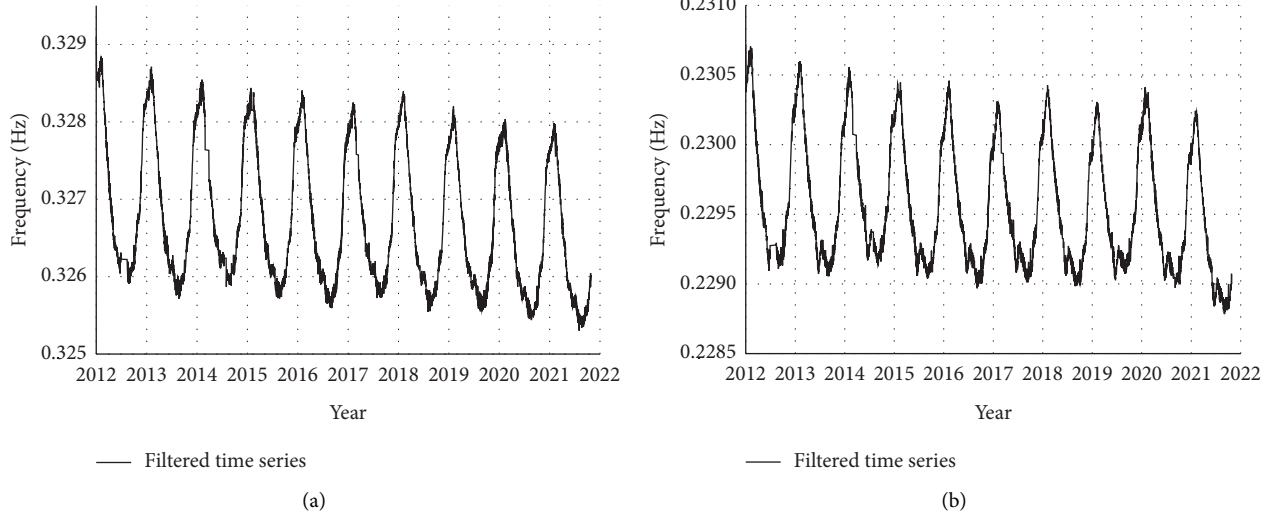


FIGURE 5: Filtered time series of modal frequencies: (a) Fourth-order symmetric torsional frequency. (b) First-order symmetric torsional frequency.

As shown in Figure 5, we use the Savitzky–Golay smoothing and differentiation filter [39] to delineate the trend of modal frequencies more prominent, where the data of estimated time series are used.

The Prophet model has the capacity to decompose the time series. In Figure 6, we decompose the times series of the modal frequency to multiple timescales. The yearly seasonality is prominent, where the modal frequency got to the maximal value around February (winter) and to the minimal value around August (summer) each year. It is strongly believed that the yearly seasonality has something to do with the yearly variation of ambient interference (variation of the temperature is the reason, which is investigated in section 5). Similarly, the daily seasonality can also be noticed due to the daily variation of ambient interference, where the maximal value is observed around 1 am and the minimal value is observed around 15 pm (the reason is similar to the yearly seasonality). The weekly seasonality has no obvious rule, which is related with the traffic condition on the bridge and varies with each individual. For most cases, the holiday effects seem to increase the modal frequencies. It is obvious that the general trend of the modal frequency is continuously decreasing. In addition, compared with the yearly seasonality, the amplitudes of the other type seasonality and holiday effects are negligible. The daily seasonality and the holiday effects are of the same amplitudes (about 10^{-4} Hz). The amplitude of the weekly seasonality is 10^{-5} Hz. The yearly seasonality has the largest amplitude, which is 10^{-3} Hz.

As shown in Figure 7, the similar rules for yearly and daily seasonality are also found in the other mode. The general trend of the modal frequency is also decreasing.

3.5.2. Decomposition for Damping Ratio. As shown in Figure 8, the black points are the identified time series of the damping ratio from the SHM system. The red points are the estimated time series reconstructed by the Prophet model. It can be noticed that from July 2019 to April 2020, the

damping ratio increased abruptly (which are found in most modes). The latent reason might be that there were some temporary measures to suppress the vibration (e.g., maintenance of expansion joints). This anomaly should be confirmed with the bridge maintainers, which is out of the scope of this paper. As a result, we only use the data from January 2012 to June 2019 for the analysis of the damping ratio. Compared with the modal frequency, the damping ratio is much more discrete. The damping ratio is also yearly fluctuating but less obvious than the modal frequency. The general trend is not significant at the first glance.

As shown in Figure 9, the similar regularity is also found in the first-order symmetric torsional mode.

Figure 10 shows the trend of damping ratios more prominently with the data of estimated time series.

Figure 11 shows the decomposed time series of damping ratios. The yearly seasonality attains the maximal value around January (winter) and the minimal value around September (summer) each year, which might be caused by the yearly fluctuating ambient interference. The daily seasonality attains the maximal value around 5 am and the minimal value around 13 pm. The weekly seasonality varies with each individual, amplitude of which is negligible compared with other types of seasonality. The holiday effects seem to decrease the damping ratio. The general trend seems to be increasing. But the damping ratio is more complicated and can be changed by man-made actions. As a result, it is hard to conclude that the natural process of damping ratio is to increase with structural usage. For the damping ratio, the amplitude of yearly seasonality is usually more significant. But the holiday effects is often of the same amplitude as the yearly seasonality. The amplitude of daily seasonality is ambiguous, which may be of the same amplitude (Figure 11) or the lower amplitude (Figure 12) as the yearly seasonality. Furthermore, the performance metric ((17)) of the damping ratio is relatively lower than that of the modal frequency, which means the daily seasonality may also be in numerical errors.

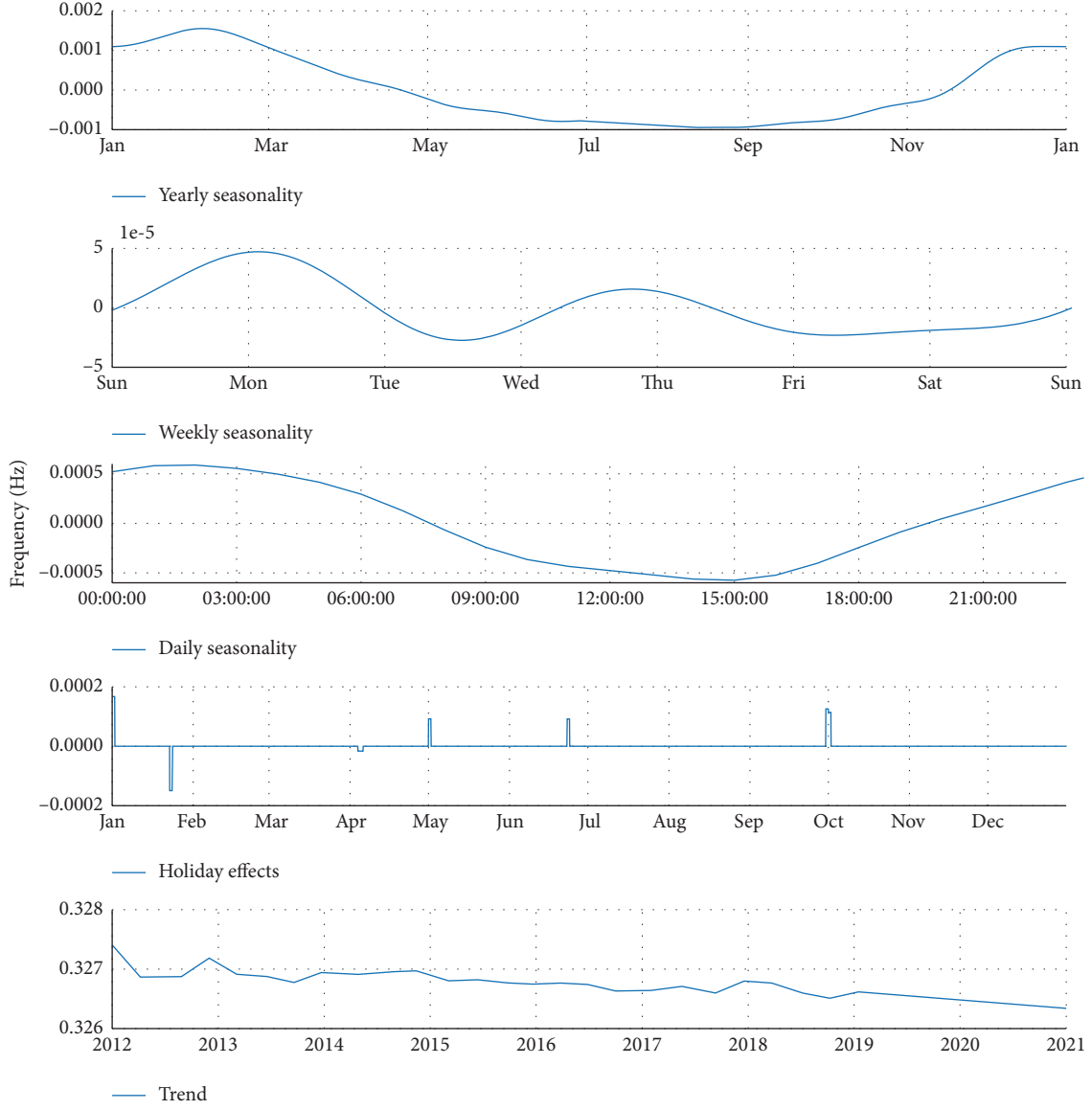


FIGURE 6: Fourth-order symmetric torsional frequency: multimescale component.

4. Long-Term Trend

According to the decomposed time series of dynamic properties, we get the long-term trend. In this section, we give the evolving regularity of modal frequencies and damping ratios.

4.1. Modal Frequency. As shown in Figure 13, the modal frequencies are prone to decrease in the long term. For the first-order symmetric torsional mode, the modal frequency decreases 0.16% (from 0.2297 to 0.2293) in 10 years according to the equation of linear regression. For the fourth-order symmetric torsional mode, the deterioration of modal frequency in 10 years is about 0.21% (from 0.3271 to 0.3264).

4.2. Damping Ratio. Figure 14 indicates that the damping ratio is likely to increase in the long term. Again, because the damping ratio can be changed by man-made action, the

extracted long-term trend is not necessary the natural evolving regularity. For the first-order symmetric torsional mode, the damping ratio increases 14% (from 0.0026 to 0.0030). The damping ratio of the fourth-order symmetric torsional mode increases 5% (from 0.0028 to 0.0029).

5. Ambient Interference

The ambient interference affects the dynamic properties greatly. In this section, we conduct the correlation analysis between the time-variant environmental conditions and the yearly seasonality of the dynamic properties, where the effects of long-term trend are excluded. The temperature and relative humidity at the 2 meter height above the sea surface are chosen as the representative ambient interference. The database of the ambient interference that we employ is from the ERA5 global reanalysis [31]. Due to the limit of spatial resolution of the database, the location of the measured data

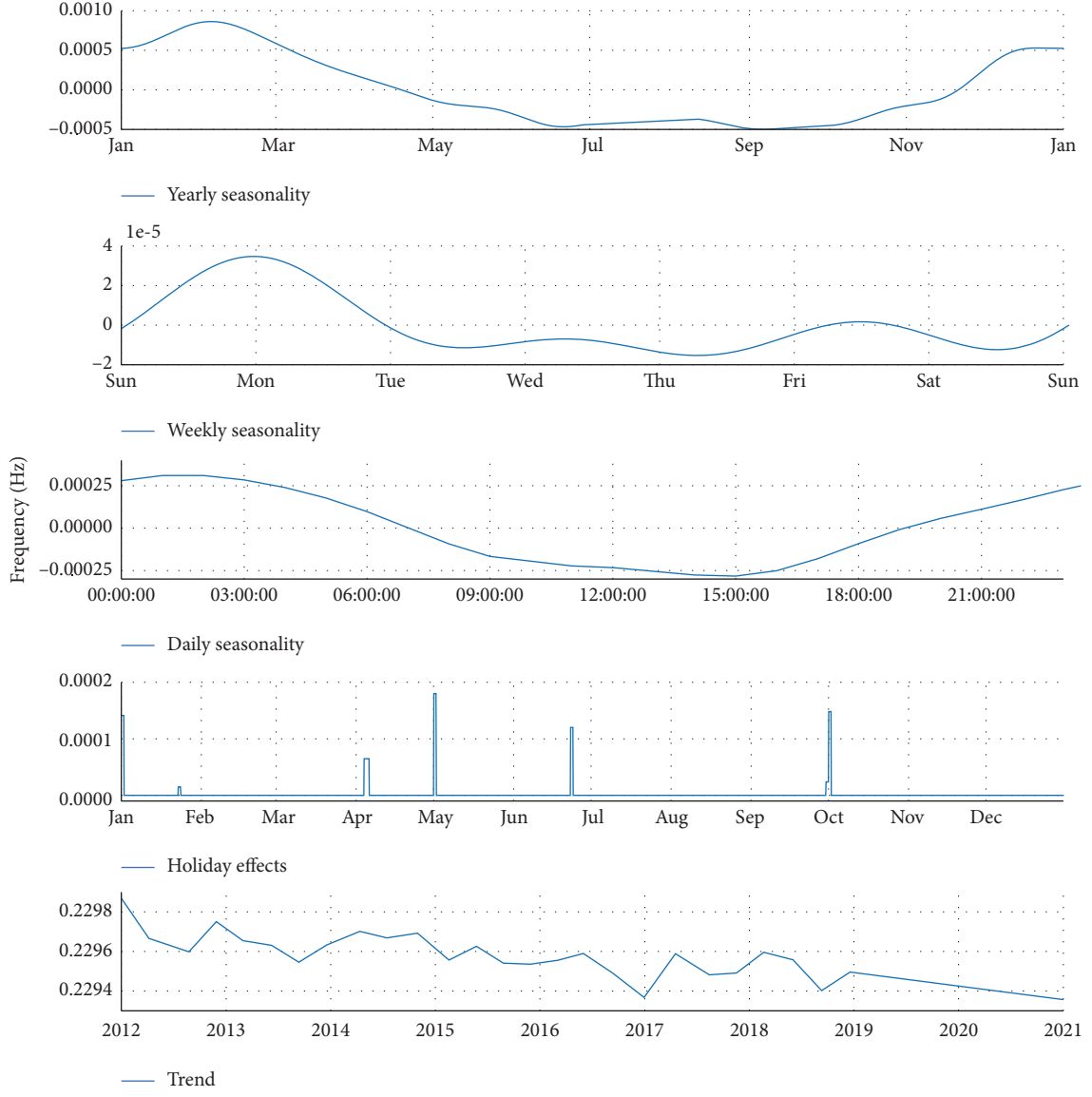


FIGURE 7: First-order symmetric torsional frequency: multitemplescale component.

is not the same as that of the bridge. As shown in Figure 1, we choose the closest point ($30^{\circ}\text{N}, 121.9^{\circ}\text{E}$) to the bridge in the database, which will not affect the results much.

5.1. Temperature. Figure 15 shows the varying temperature at the 2-meter height above the sea surface from 2012 to 2022 at the location of $30^{\circ}\text{N}, 121.9^{\circ}\text{E}$.

5.1.1. Modal Frequency. Figure 16 indicates that the temperature and the yearly seasonality of the modal frequency have a strong correlation. The frequency will decrease if the temperature increases. For the first-order symmetric torsional mode, the modal frequency will approximately decrease by 0.82×10^{-4} Hz if the temperature increases by 1°C . For the fourth-order symmetric torsional mode, the modal frequency will approximately decrease by 1.49×10^{-4} Hz if the temperature increases by

1°C . The conclusions above are valid when the temperature is $0 - 25^{\circ}\text{C}$. Recalling the general deterioration of modal frequencies (Figure 13), it is found that the variations caused by natural deterioration and temperature are of the same amplitude, both 10^{-4} .

5.1.2. Damping Ratio. Figure 17 shows that the damping ratio will decrease with the increment of temperature in general. Compared with the modal frequency, however, the temperature and damping ratio are not one-to-one relationship. For example, Figure 17(a) shows that both 3°C and 10°C correspond the variation of the damping ratio by 2×10^{-4} .

5.2. Relative Humidity. Figure 18 shows the varying relative humidity at the 2 meter height above the sea surface from 2012 to 2022 at the location of $30^{\circ}\text{N}, 121.9^{\circ}\text{E}$.

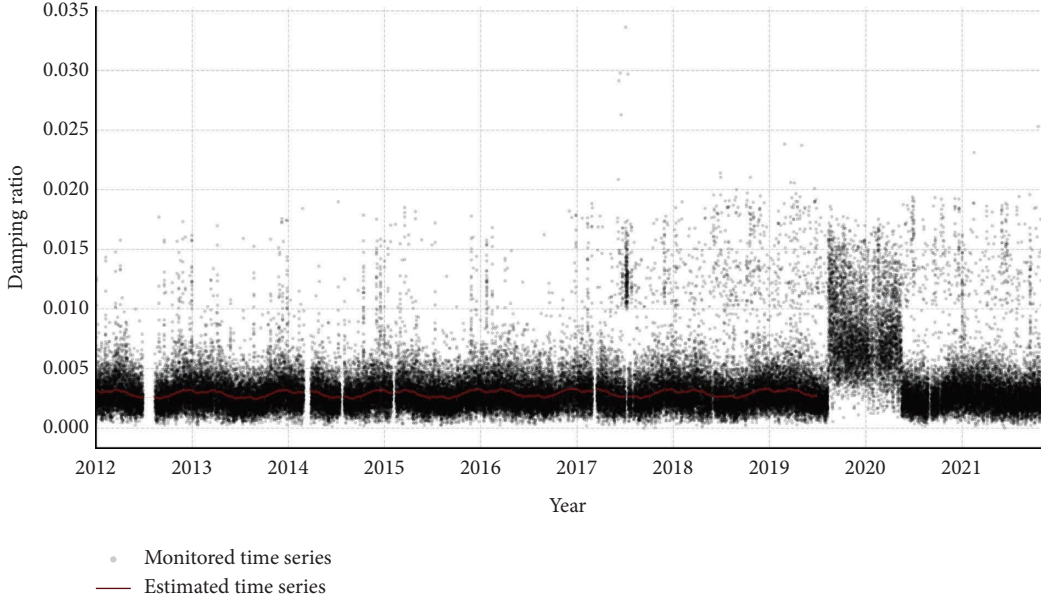


FIGURE 8: Fourth-order symmetric torsional damping ratio: monitored time series and estimated time series ($M = 0.1874$).

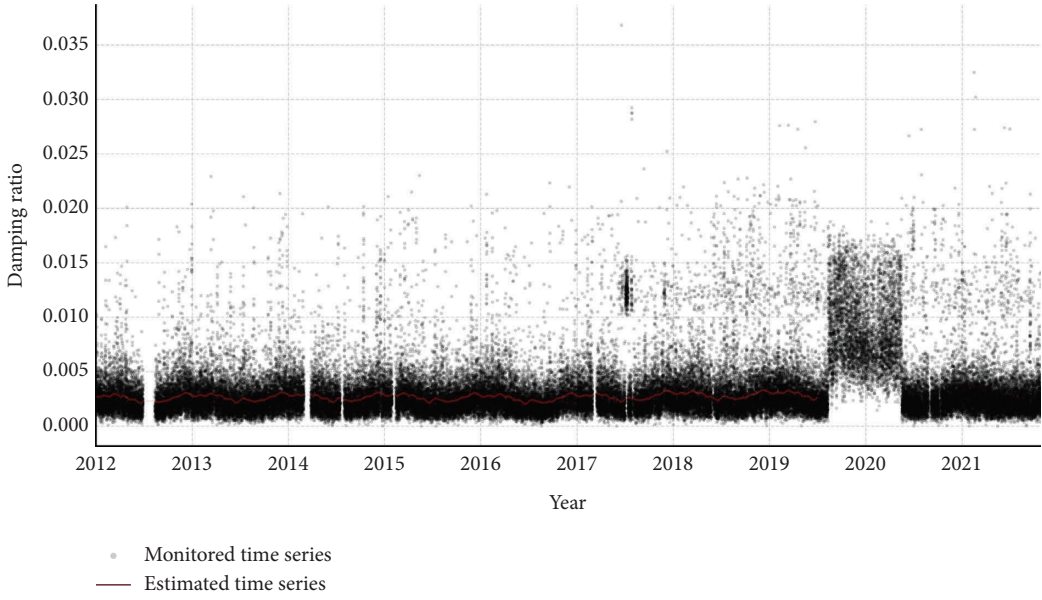


FIGURE 9: First-order symmetric torsional damping ratio: monitored time series and estimated time series ($M = 0.2068$).

5.2.1. Modal Frequency. For the modal frequency, the relative humidity seems to have nothing to do with the yearly seasonality of the modal frequency, as shown in Figure 19.

5.2.2. Damping Ratio. As shown in Figure 20, there is no significant correlation between the relative humidity and the yearly seasonality of the damping ratio as well.

6. Distribution of Model Errors

Model errors are the residuals between the estimated values and the measured values, which are mainly caused by improper model assumptions.

For the modal frequency, the normal distribution is used to fit model errors as shown in Figure 21 (Table 2).

$$f(x) = \frac{1}{\sigma\sqrt{2\pi}} e^{-(1/2)(x-\mu/\sigma)^2}, \quad (18)$$

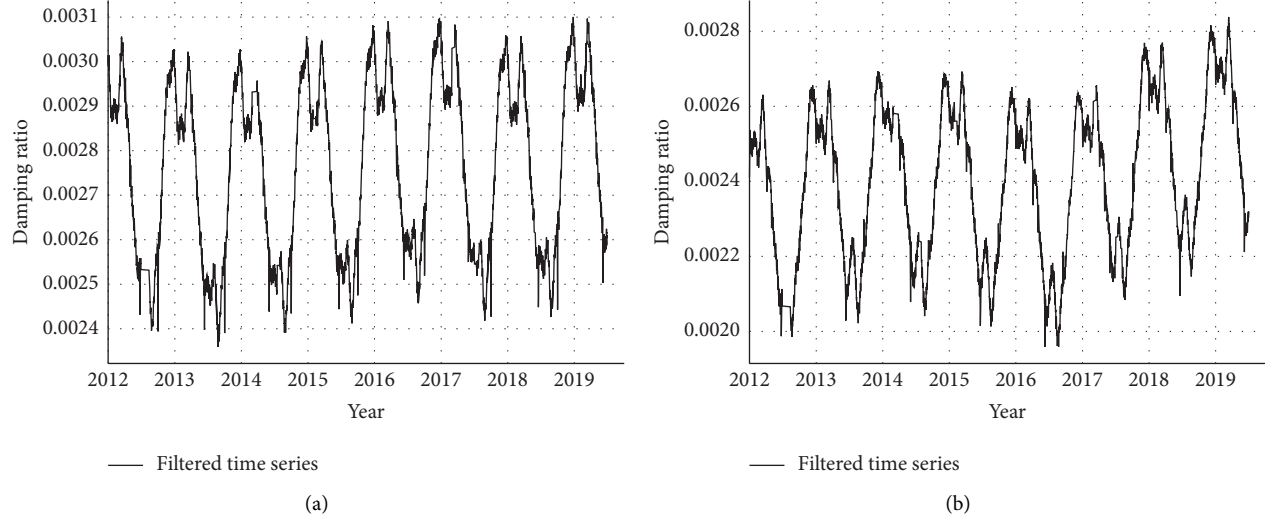


FIGURE 10: Filtered time series of damping ratio: (a) Fourth-order symmetric torsional damping ratio. (b) First-order symmetric torsional damping ratio.

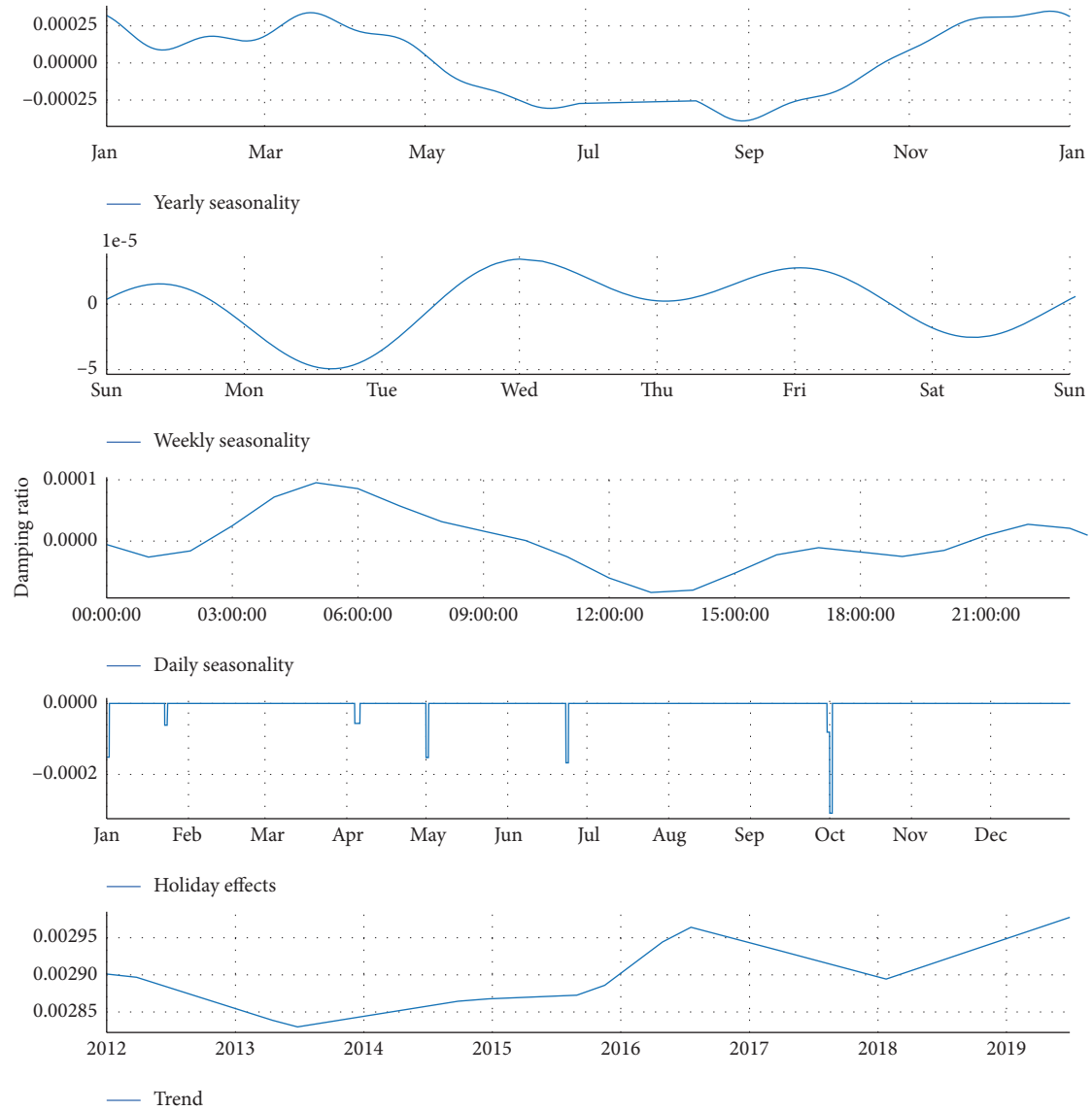


FIGURE 11: Fourth-order symmetric torsional damping ratio: multitimescale component.

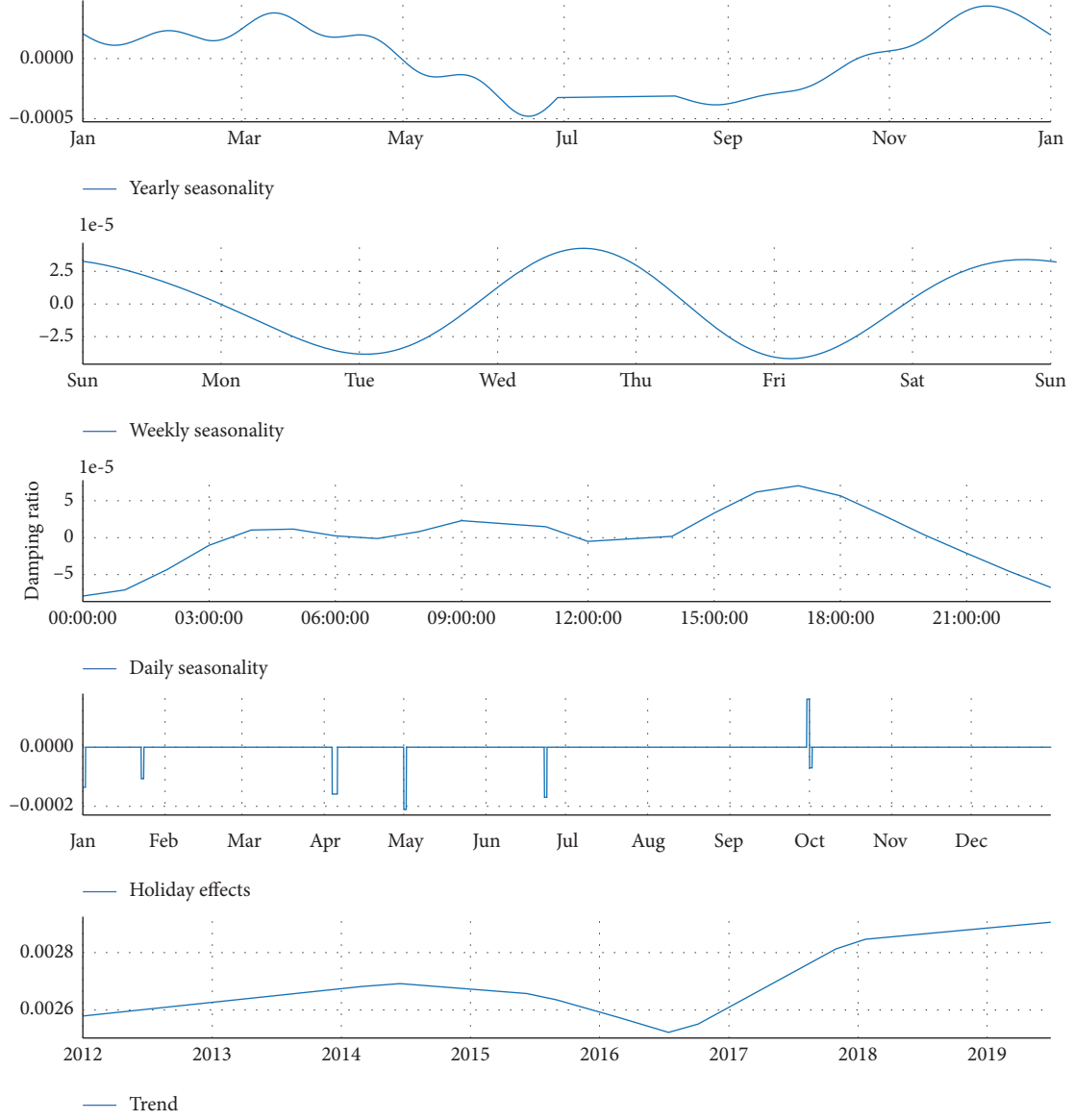


FIGURE 12: First-order symmetric torsional damping ratio: multimescale component.

where σ is the standard variance, μ is the mean value, and $f(\cdot)$ is the PDF.

For the damping ratio, we use the bimodal normal distribution to fit model errors as shown in Figure 22 (Table 3).

$$f(x) = \frac{pA}{\sigma_1 \sqrt{2\pi}} \exp \left[-\frac{1}{2} \left(\frac{x - \mu_1}{\sigma_1} \right)^2 \right] + \frac{(1-p)A}{\sigma_2 \sqrt{2\pi}} \exp \left[-\frac{1}{2} \left(\frac{x - \mu_2}{\sigma_2} \right)^2 \right], \quad (19)$$

where μ_i and σ_i are the mean value and standard variation ($i = 1, 2$); p and $1 - p$ are the weights of bimodal models; and A is the normalized coefficient.

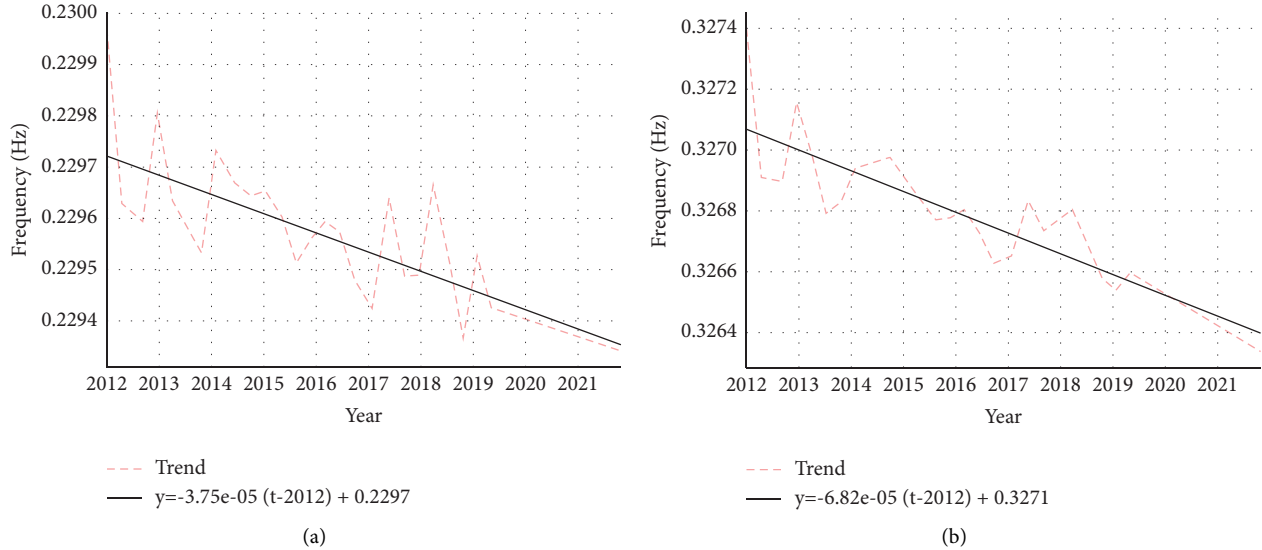


FIGURE 13: Long-term trend of modal frequency: (a) first-order symmetric torsional mode; (b) fourth-order symmetric torsional mode.

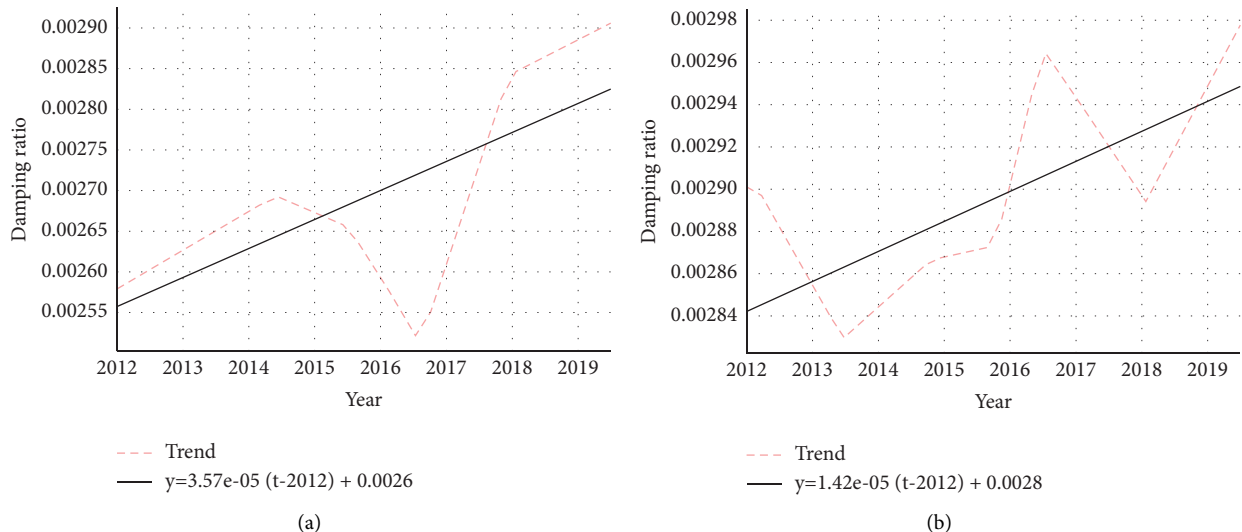


FIGURE 14: Long-term trend of damping ratio: (a) first-order symmetric torsional mode; (b) fourth-order symmetric torsional mode.

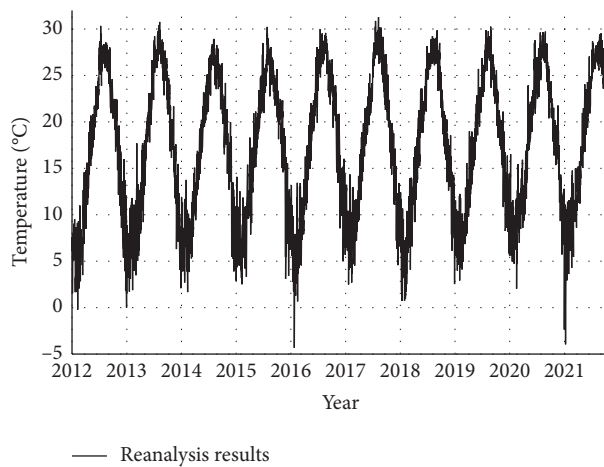


FIGURE 15: Temperature at the 2-meter height above the sea surface (30°N , 121.9°E).

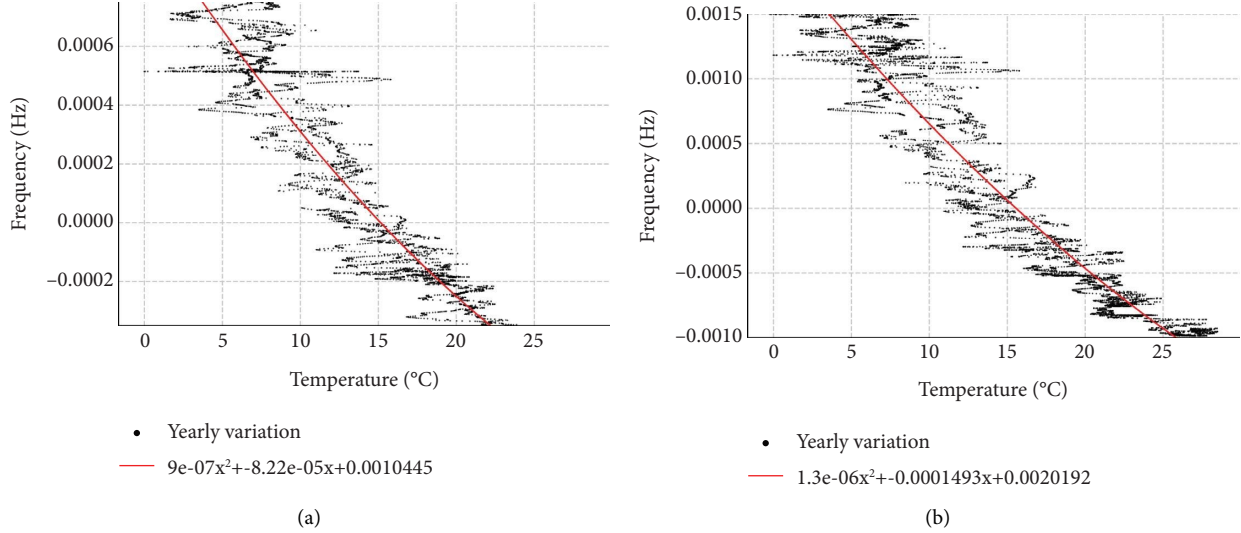


FIGURE 16: Relationship between temperature and modal frequency's yearly seasonality: (a) first-order symmetric torsional mode; (b) fourth-order symmetric torsional mode.

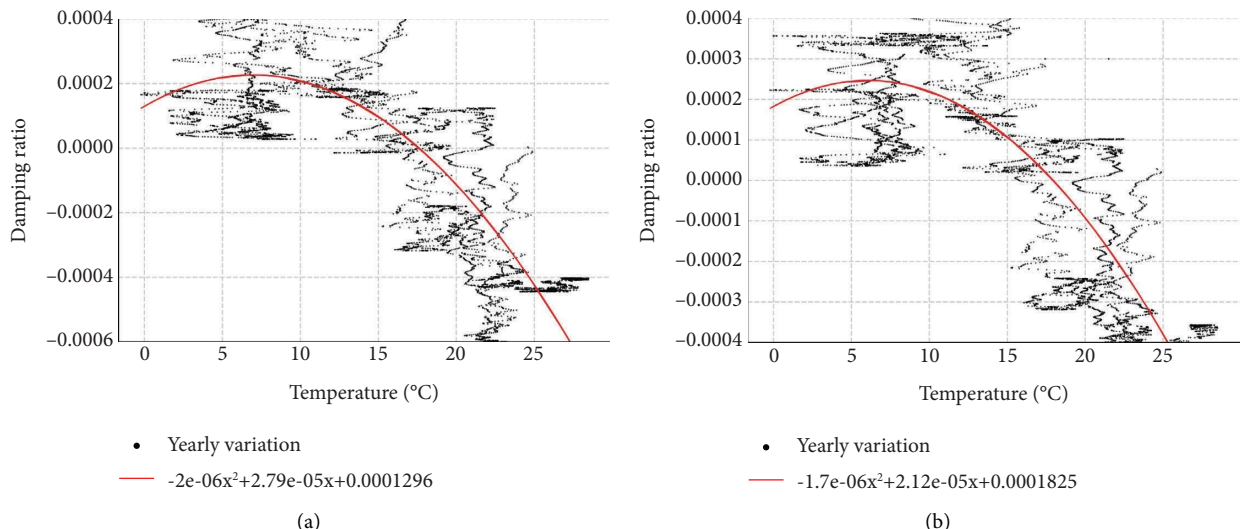


FIGURE 17: Relationship between temperature and damping ratio's yearly seasonality: (a) first-order symmetric torsional mode; (b) fourth-order symmetric torsional mode.

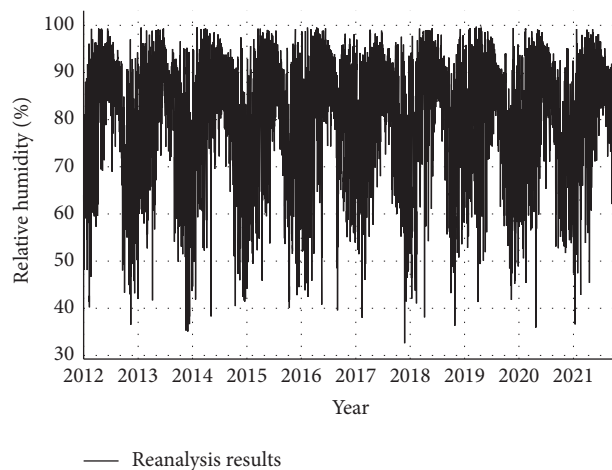


FIGURE 18: Relative humidity at the 2 meter height above the sea surface (30°N, 121.9°E).

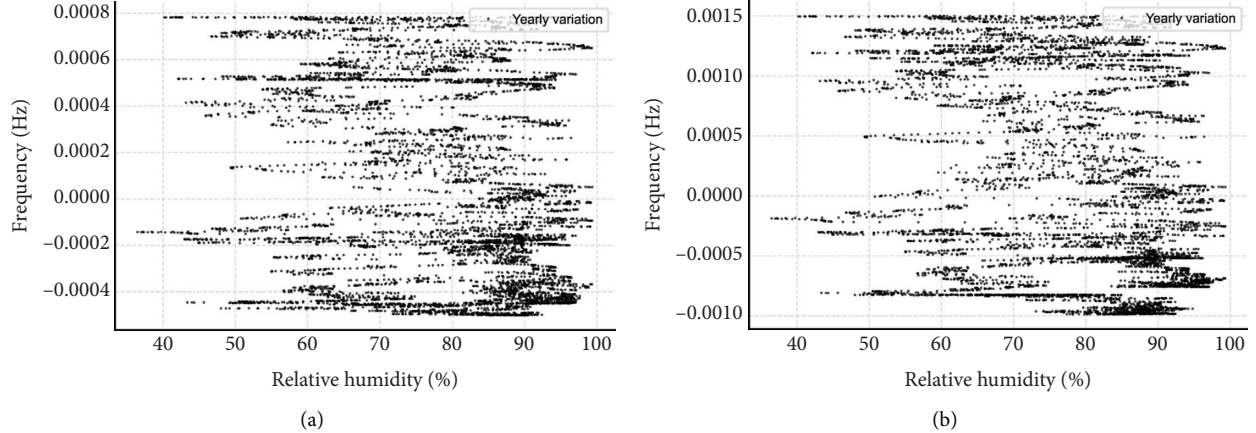


FIGURE 19: Relationship between relative humidity and modal frequency's yearly seasonality: (a) first-order symmetric torsional mode; (b) fourth-order symmetric torsional mode.

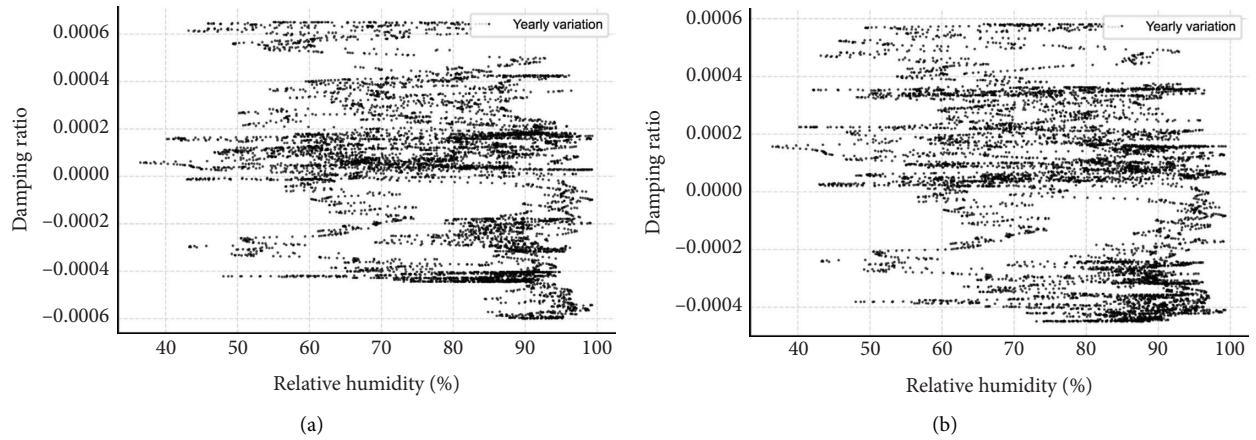


FIGURE 20: Relationship between relative humidity and damping ratio's yearly seasonality: (a) first-order symmetric torsional mode; (b) fourth-order symmetric torsional mode.

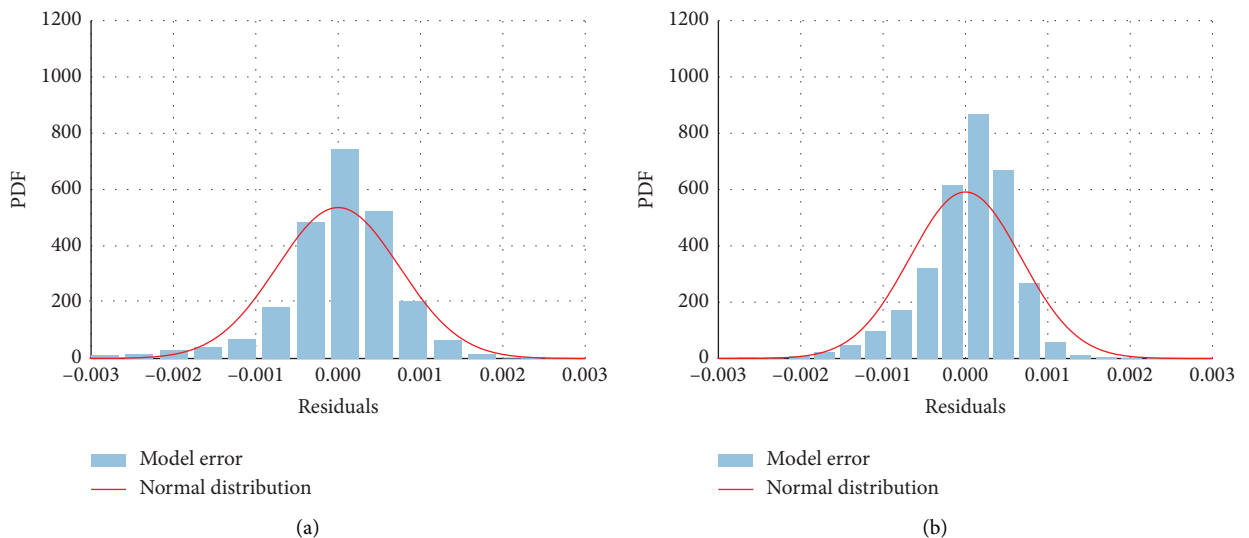


FIGURE 21: Histogram of model error for frequencies. (a) Fourth-order symmetric torsional mode. (b) First-order symmetric torsional mode.

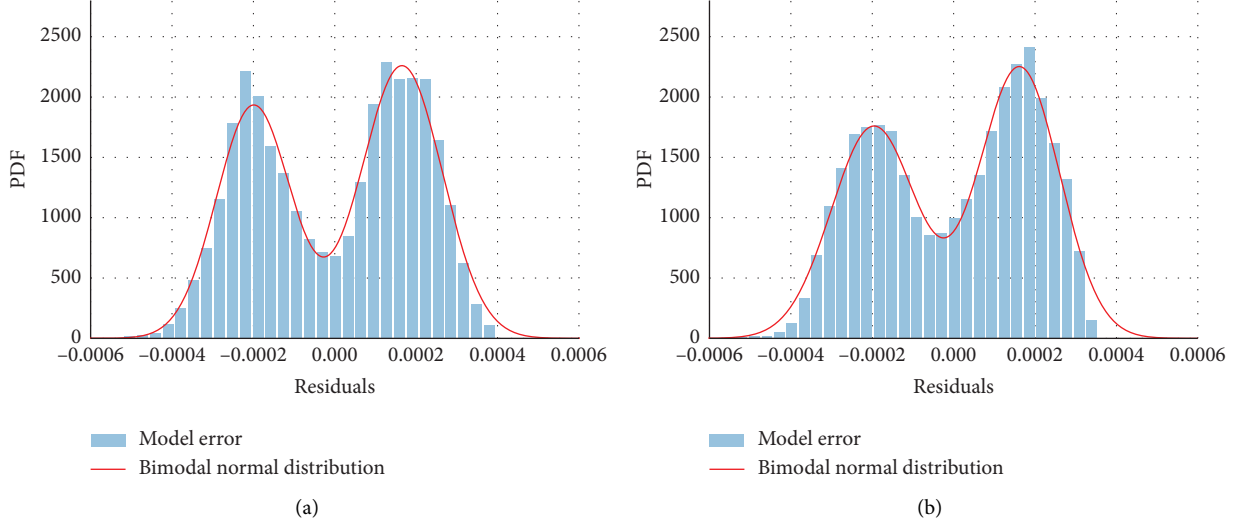


FIGURE 22: Histogram of model error for damping ratios. (a) Fourth-order symmetric torsional mode. (b) First-order symmetric torsional mode.

TABLE 2: Distribution parameters for modal frequencies.

Mode	σ	μ
4-ST	7.44×10^{-4}	-2.38×10^{-8}
1-ST	6.74×10^{-4}	-2.43×10^{-8}

TABLE 3: Distribution parameters for damping ratios.

Mode	σ_1	μ_1	σ_2	μ_2	p	A
4-ST	-1.99×10^{-4}	9.12×10^{-5}	1.65×10^{-4}	9.96×10^{-5}	0.4391	1.0053
1-ST	-1.96×10^{-4}	1.05×10^{-4}	1.62×10^{-4}	9.86×10^{-5}	0.4530	1.0160

7. Conclusions

In order to distinguish the long-term and periodic effects of structural dynamic properties, this article proposes an interpretable methodology to decompose the time series into long-term parts, multiscale periodic parts, holiday parts, and model errors. By analyzing the long-term parts, we can conclude that the modal frequencies are decreasing with the structural usage (about 0.20% each decade), which reflect the effects of structural deterioration. The damping ratios seem to increase in the long term. However, the damping ratios can be influenced by exterior conditions (e.g., structural maintenance, tuned mass damper, and wind velocity). So, the long-term varying rules of the structural damping still need to be investigated in the future. By analyzing the relationship between multiscale periodic parts and ambient environmental conditions, we find that the increment of temperature can decrease the modal frequencies and damping ratios. For modal frequencies, the variations caused by natural deterioration and temperature are of the same amplitudes (10^{-4}). Differently, for buildings, the increment of temperature can increase the modal frequencies, which means the underlying mechanics between the modal frequencies and temperatures can be complicated. For the varying reasons of long-span bridges, a possible explanation

is that the higher temperature will loosen the cables and the loose cables decrease the stiffness (i.e., the modal frequencies). For buildings, the varying phenomenon may be caused by temperature-sensitive material properties. Due to the limit of data acquisition, we did not discuss the relationship among cable forces, cable temperatures, and modal frequencies, which needs to be investigated further in future researches. As for the humidity, this paper does not find its reasonable relationship with structural dynamic properties.

In a nutshell, this article investigates to what extent the structural deterioration and the ambient environmental conditions can change the structural dynamic properties, which provide a reference for damage detection and safety assessment of similar long-span bridges.

Data Availability

The data used to support the findings of the study are available from the corresponding author upon reasonable request.

Additional Points

10-year dynamic properties of a long-span bridge are investigated. A multiscale time series decomposition methodology is used to distinguish long-term and periodic effects.

Frequencies will decrease in the long term but damping ratios will increase. The increment of temperature will lead to the decrease for both frequencies and damping ratios. Dynamic properties are not significantly related with humidity.

Conflicts of Interest

The authors declare that they have no conflicts of interest.

Authors' Contributions

Xiaolei Chu wrote the original draft, conceptualized, investigated, validated, and visualized the study, performed formal analysis, and developed methodology. Wei Cui was involved in conceptualized and supervised the study, reviewed and edited the manuscript, and involved in funding acquisition. Shengyi Xu developed methodology. Lin Zhao was responsible for funding acquisition. Hua Guan acquired data. Yaojun Ge was responsible for supervision and funding acquisition.

Acknowledgments

The authors gratefully acknowledge the support of the National Key Research and Development Program of China (2021YFF0502200) and National Natural Science Foundation of China (52008314 and 51978527).

References

- [1] R. Brincker, L. Zhang, and P. Andersen, "Modal identification of output-only systems using frequency domain decomposition," *Smart Materials and Structures*, vol. 10, no. 3, pp. 441–445, 2001.
- [2] Z. Peng, P. W. Tse, and F. Chu, "An improved hilbert–huang transform and its application in vibration signal analysis," *Journal of Sound and Vibration*, vol. 286, no. 1-2, pp. 187–205, 2005.
- [3] J. X. Mao, H. Wang, D. M. Feng, T. Y. Tao, and W. Z. Zheng, "Investigation of dynamic properties of long-span cable-stayed bridges based on one-year monitoring data under normal operating condition," *Structural Control and Health Monitoring*, vol. 25, no. 5, p. e2146, 2018.
- [4] L. Hermans and H. Van der Auweraer, "Modal testing and analysis of structures under operational conditions: industrial applications," *Mechanical Systems and Signal Processing*, vol. 13, no. 2, pp. 193–216, 1999.
- [5] J. L. Beck, "Bayesian system identification based on probability logic," *Structural Control and Health Monitoring*, vol. 17, no. 7, pp. 825–847, 2010.
- [6] L. S. Katafygiotis and K. V. Yuen, "Bayesian spectral density approach for modal updating using ambient data," *Earthquake Engineering and Structural Dynamics*, vol. 30, no. 8, pp. 1103–1123, 2001.
- [7] K. V. Yuen and L. S. Katafygiotis, "Bayesian fast fourier transform approach for modal updating using ambient data," *Advances in Structural Engineering*, vol. 6, no. 2, pp. 81–95, 2003.
- [8] S. K. Au, "Fast bayesian FFT method for ambient modal identification with separated modes," *Journal of Engineering Mechanics*, vol. 137, no. 3, pp. 214–226, 2011.
- [9] S. K. Au, "Fast bayesian ambient modal identification in the frequency domain, part i: posterior most probable value," *Mechanical Systems and Signal Processing*, vol. 26, pp. 60–75, 2012.
- [10] X. Chu, W. Cui, P. Liu, L. Zhao, and Y. Ge, "Bayesian spectral density approach for identification of bridge section's flutter derivatives operated in turbulent flow," *Mechanical Systems and Signal Processing*, vol. 170, Article ID 108782, 2022.
- [11] W. J. Yan, Z. Q. Feng, W. Yang, and K. V. Yuen, "Bayesian inference for the dynamic properties of long-span bridges under vortex-induced vibration with scanlan's model and dense optical flow scheme," *Mechanical Systems and Signal Processing*, vol. 174, Article ID 109078, 2022.
- [12] P. Liu, X. Chu, W. Cui, L. Zhao, and Y. Ge, "Bayesian inference based parametric identification of vortex-excited force using on-site measured vibration data on a long-span bridge," *Engineering Structures*, vol. 266, Article ID 114597, 2022.
- [13] O. Salawu, "Detection of structural damage through changes in frequency: a review," *Engineering Structures*, vol. 19, no. 9, pp. 718–723, 1997.
- [14] Y. Ge, L. Zhao, and J. Cao, "Case study of vortex-induced vibration and mitigation mechanism for a long-span suspension bridge," *Journal of Wind Engineering and Industrial Aerodynamics*, vol. 220, Article ID 104866, 2022.
- [15] L. Zhao, W. Cui, X. Shen, S. Xu, Y. Ding, and Y. Ge, "A fast on-site measure-analyze-suppress response to control vortex-induced-vibration of a long-span bridge," in *Structures*, vol. 35, pp. 192–201, Elsevier, 2022.
- [16] J. Zhang, L. Zhou, Y. Tian, S. Yu, W. Zhao, and Y. Cheng, "Vortex-induced Vibration Measurement of a Long-Span Suspension Bridge through Noncontact Sensing Strategies," *Computer-Aided Civil and Infrastructure Engineering*, vol. 37, no. 12, pp. 1617–1633, 2021.
- [17] K. V. Yuen and S. C. Kuok, "Ambient interference in long-term monitoring of buildings," *Engineering Structures*, vol. 32, no. 8, pp. 2379–2386, 2010.
- [18] H. Li, S. Li, J. Ou, and H. Li, "Modal identification of bridges under varying environmental conditions: temperature and wind effects," *Structural Control and Health Monitoring*, vol. 17, no. 5, pp. 495–512, 2010.
- [19] D. Anastopoulos, G. De Roeck, and E. P. Reynders, "One-year operational modal analysis of a steel bridge from high-resolution macrostrain monitoring: influence of temperature vs. retrofitting," *Mechanical Systems and Signal Processing*, vol. 161, Article ID 107951, 2021.
- [20] D. Hwang, S. Kim, and H. K. Kim, "Long-term damping characteristics of twin cable-stayed bridge under environmental and operational variations," *Journal of Bridge Engineering*, vol. 26, no. 9, Article ID 4021062, 2021.
- [21] A. Kareem and Y. Tamura, *Advanced structural wind engineering*, Vol. 482, Springer, Berlin, Germany, 2013.
- [22] M. Novak and L. E. Hifnawy, "Effect of soil-structure interaction on damping of structures," *Earthquake Engineering and Structural Dynamics*, vol. 11, no. 5, pp. 595–621, 1983.
- [23] J. Dai, Z. D. Xu, X. J. Yin, P. P. Gai, and Y. Luo, "Parameters design of tmd mitigating vortex-induced vibration of the Hong Kong–zhuhai–Macao bridge deep-water nonnavigable bridge," *Journal of Bridge Engineering*, vol. 24, no. 8, Article ID 6019005, 2019.
- [24] P. Omenzetter and J. M. W. Brownjohn, "Application of time series analysis for bridge monitoring," *Smart Materials and Structures*, vol. 15, no. 1, pp. 129–138, 2006.

- [25] L. Yu and J. C. Lin, "Cloud computing-based time series analysis for structural damage detection," *Journal of Engineering Mechanics*, vol. 143, no. 1, p. C4015002, 2017.
- [26] K. Kumar, P. K. Biswas, and N. Dhang, "Time series-based shm using pca with application to asce benchmark structure," *Journal of Civil Structural Health Monitoring*, vol. 10, no. 5, pp. 899–911, 2020.
- [27] O. R. de Lautour and P. Omenzetter, "Damage classification and estimation in experimental structures using time series analysis and pattern recognition," *Mechanical Systems and Signal Processing*, vol. 24, no. 5, pp. 1556–1569, 2010.
- [28] M. Gul and F. Necati Catbas, "Statistical pattern recognition for structural health monitoring using time series modeling: theory and experimental verifications," *Mechanical Systems and Signal Processing*, vol. 23, no. 7, pp. 2192–2204, 2009.
- [29] S. J. Taylor and B. Letham, "Forecasting at scale," *The American Statistician*, vol. 72, no. 1, pp. 37–45, 2018.
- [30] A. C. Harvey and S. Peters, "Estimation procedures for structural time series models," *Journal of Forecasting*, vol. 9, no. 2, pp. 89–108, 1990.
- [31] H. Hersbach, B. Bell, P. Berrisford et al., "The era5 global reanalysis," *Quarterly Journal of the Royal Meteorological Society*, vol. 146, no. 730, pp. 1999–2049, 2020.
- [32] K. V. Yuen, *Bayesian Methods for Structural Dynamics and Civil Engineering*, John Wiley and Sons, Hoboken, NJ, USA, 2010.
- [33] P. J. Van Laarhoven and E. H. Aarts, "Simulated annealing," in *Simulated Annealing: Theory and Applications*, pp. 7–15, Springer, Berlin, Germany, 1987.
- [34] C. Andrieu, N. De Freitas, A. Doucet, and M. I. Jordan, "An introduction to mcmc for machine learning," *Machine Learning*, vol. 50, no. 1/2, pp. 5–43, 2003.
- [35] S. K. Au, *Operational Modal Analysis*, Springer, Berlin, Germany, 2017.
- [36] Y. Yang, T. Ma, and Y. Ge, "Evaluation on bridge dynamic properties and viv performance based on wind tunnel test and field measurement," *Wind and Structures*, vol. 20, no. 6, pp. 719–737, 2015.
- [37] A. C. Harvey and N. Shephard, "10 Structural Time Series Models 1993," *Handbook of Statistics*, vol. 11, pp. 261–302, 1993.
- [38] Q. W. Zhang, L. C. Fan, and W. C. Yuan, "Traffic-induced variability in dynamic properties of cable-stayed bridge," *Earthquake Engineering and Structural Dynamics*, vol. 31, no. 11, pp. 2015–2021, 2002.
- [39] W. H. Press and S. A. Teukolsky, "Savitzky-golay smoothing filters," *Computers in Physics*, vol. 4, no. 6, pp. 669–672, 1990.